Influence of anchoring in the phase behaviour of discotic liquid crystals

Daniel Salgado-Blanco, †[a] Carlos I. Mendoza,[b] Marco A. Chávez-Rojo,[c] José A. Moreno-Razo[a] and Enrique Díaz-Herrera*[a]

Molecular dynamics simulations were performed for a Gay-Berne discotic fluid confined in a slab geometry for two different anchorings: homeotropic (face-on) and planar (edge-on), and for two different confinement lengths. Our results show that the behaviour of the more confined system in the temperature region of the isotropic–nematic transition is critically influenced by the presence of the walls: the growth of the solid–liquid crystal interface spans over the entire width of the cell, and the character of the transition is changed from first order to continuous. For all the confined systems studied, we observe a higher nematic–columnar transition temperature and a smaller nematic phase region in the phase diagram, as compared with the behaviour of the infinite system.

1 Introduction

When gases or liquids are adsorbed in narrow pores or capillaries, their properties may present significant changes from those observed in a bulk phase.[1,2] These confinement-induced effects on the bulk properties of a fluid are of great interest from a theoretical point of view,[3,4] as well as due to its primary importance in many industrial processes.[5] Consequently, the aim of complete understanding of dynamical and thermodynamical properties of fluids under confinement has motivated many experimental, theoretical and computational studies. In particular, computer simulations have played an important role in the understanding of confined systems, mainly because they allow the spatial behaviour to be characterized in a detail that is not always possible to achieve with experiments, or can deal with systems that are too complex to be analyzed with theoretical methods only.

Independently of the type of particles forming a fluid, the walls in a spatially confined system locally induce a positional order, which results in a stratification of the fluid. For a fluid composed of anisotropic particles, the walls impose a constraint not only in their position but also in their orientation,

which results in the modification of the mesophases formed.[6–8] Such is the case of confined liquid crystals (LC), where the breaking of the symmetry of the system, due to confinement, modifies the structure of the liquid crystal phase for two main reasons: first, those nematogens whose orientation is frustrated by the wall result in a perturbation of the original, unbounded LC phase, creating an interface between it and the solid (wall), and, second, far from this interface the bulk of the LC is recovered, but with a preferred orientation that is promoted by the particles at the interface, as the elastic forces tend to orient all the molecules parallel to each other.[6]

Confinement is critical to many LC technologies,[9–11] such as in the cases of displays and optical switches. Although different numerical studies have been performed to understand the different parameters involved in this process where the LCs are forced to arrange themselves, or self-assemble, under conditions of confinement, most of them have been dedicated to the case of a fluid composed of rod-like molecules (prolates),[12–15] and few of them have focused on the effect of confining a discotic liquid crystal (oblates).[16–18] A discotic liquid crystal (DLC) consists of disc-shaped mesogens that have the ability to arrange forming structures with long-range order such as nematic or columnar phases. This latter phase, coupled with their promising charge carrier mobilities and the fact that they can be considered as organic semiconductors, make DLCs a particularly interesting candidate for applications in the photovoltaic industry.[19] Nevertheless, more attention is needed to complete design principles for DLCs in a confined environment that improve the handling of their orientational order.

A common strategy to achieve a desired orientation, or improve the orientational order in confined LC systems, in general, is by means of anchoring on the walls, that is, by the

[a] Departamento de Física, Universidad Autónoma Metropolitana-Iztapalapa, Ave. San Rafael Atlixco 186, Col. Vicentina, 09340 México, Ciudad de México, Mexico. E-mail: diaz@xanum.uam.mx

[b] Instituto de Investigaciones en Materiales, Universidad Nacional Autónoma de México, Apdo. Postal 70-360, 04510 México, Ciudad de México, Mexico

[c] Facultad de Ciencias Químicas, Universidad Autónoma de Chihuahua, Venustiano Carranza S/N, 31000 Chihuahua, Chihuahua, Mexico

† Present address: Centro Nacional de Supercómputo, Instituto Potosino de Investigación Científica y Tecnológica, Camino a la Presa San José 2055, 78216, San Luis Potosí, México. E-mail: daniel.salgado@ipicyt.edu.mx
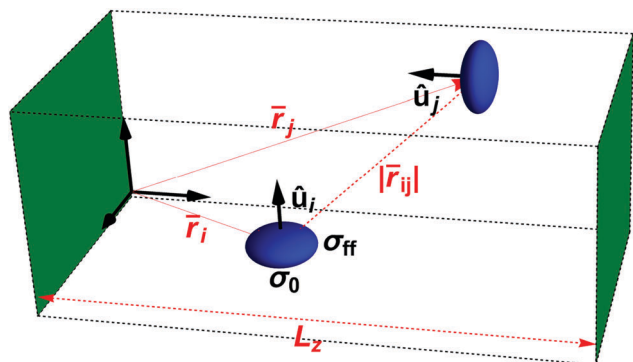
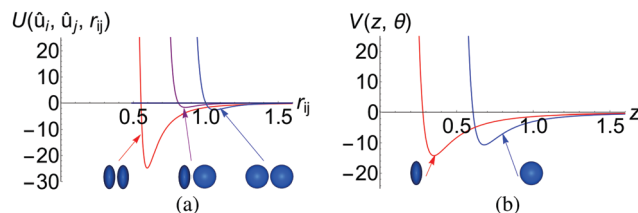**Fig. 1** Schematic view of the system under study.

Fig. 2 (a) Disc–disc interaction potential as given by eqn (1) for the system GB(0.5, 0.2, 1.0, 2.0). The red line corresponds to the face–face interaction, the blue line to the edge–edge interaction and the purple line to the edge–face interaction. A schematic view of a pair of discogens interacting is included in the same order in which the lines of the potential appear (from left to right: face–face, edge–face and edge–edge). (b) Wall–disc interaction potential as given by eqn (10) with the parameters set in this study. The red line corresponds to a particle in a face-on configuration ($\theta = \pi/2$) approaching a wall promoting face-on anchoring ($A = 1.0$), while the blue line corresponds to a particle in an edge-on configuration ($\theta = 0.0$) approaching a wall promoting edge-on anchoring ($A = -0.5$).

manipulation of the local order of particles adsorbed onto solid surfaces that in return induce such an order in the rest of the fluid. Such alignment of LCs can be controlled by many methods which include photoalignment techniques,[20] surface chemistry[21] and topographic patterning,[22] only to name a few. Two broad classes of anchorings can be used to describe the type of alignment: planar and homeotropic. In the first case, the director is parallel to the surface, while homeotropic anchoring means that the director lies normal to the surface. In the specific case of a confined DLC, homeotropic anchoring describes a situation where the discs lie "face-on" on the surface, and in planar anchoring they lie "edge-on" on the surface.

The main interest of this work coheres with the premise of obtaining a detailed description of the inhomogeneities arising by confining a DLC between two parallel walls (slab geometry), and compares the confined system with the phase behaviour of the same DLC fluid without the presence of the walls. Of particular importance for the present study is the work by Bellier-Castella *et al.*,[16] where the authors introduce a wall–disc interaction potential, in order to study the effects of walls promoting anchoring in a confined fluid of DLCs. In our case, we are addressing again such a question with a different approach: we are studying the system with an ensemble that allowed us to fix the distance between the walls, independently of the temperature of the system. This allowed us to report the changes in the phase behaviour of a DLC fluid when confined with walls at fixed positions, and for a given anchoring.

The rest of the paper is structured as follows: Section 2 presents the model used to mathematically describe our system and the details of the molecular simulation employed. Section 3 contains the results for all the confined systems studied in this work and the corresponding results for the unbounded system. Finally, the concluding remarks are included in Section 4.

2 Model description and simulations

2.1 Disc–disc and disc–wall interaction

The system consists of a discotic liquid crystal confined in a rectangular slab, whose walls are separated by a fixed distance $L_z{}^* = L_z/\sigma_0$ (where σ_0 is a length energy unit to be defined later),

as seen in Fig. 1. The particle–particle interaction is defined by a Gay-Berne pair potential[23]

$$U(\hat{\mathbf{u}}_i, \hat{\mathbf{u}}_j, \hat{\mathbf{r}}_{ij}) = 4\varepsilon(\hat{\mathbf{u}}_i, \hat{\mathbf{u}}_j, \hat{\mathbf{r}}_{ij})(\Xi_{ij}^{-12} + \Xi_{ij}^{-6}), \qquad (1)$$

where $\hat{\mathbf{r}}_{ij} = \mathbf{r}_{ij}/r_{ij}$ is the unit vector that connects the centers of particles i and j, $\hat{\mathbf{u}}_x$ is the unit vector along the principal axes of discogen x, and ε is the strength anisotropy function (see later). In the last expression, Ξ is an orientation dependent function defined by

$$\Xi_{ij} = \frac{\sigma_{\mathrm{ff}}}{r_{ij} - \sigma(\mathbf{u}_i, \hat{\mathbf{u}}_j, \hat{\mathbf{r}}_{ij}) + \sigma_{\mathrm{ff}}}, \qquad (2)$$

where σ_{ff} represents the thickness of the discogen. The contact distance between particles i and j is given by

$$\sigma(\hat{\mathbf{u}}_i, \hat{\mathbf{u}}_j, \hat{\mathbf{r}}_{ij}) = \sigma_0 \Gamma^{-\frac{1}{2}}(\chi) \qquad (3)$$

where the molecular anisotropy parameter, χ, is defined as

$$\chi = \frac{\kappa^2 - 1}{\kappa^2 + 1} \qquad (4)$$

with $\kappa = \sigma_{\mathrm{ff}}/\sigma_0$ and σ_0 is the diameter of the discogen. The function $\Gamma(\omega)$ is defined by

$$\Gamma(\omega) = 1 - \omega\left[\frac{c_i^2 + c_j^2 - 2\omega c_i c_j c_{ij}}{1 - \omega^2 c_{ij}^2}\right], \qquad (5)$$

with $c_i \equiv \mathbf{u}_i \cdot \hat{\mathbf{r}}_{ij}$, $c_j \equiv \mathbf{u}_j \cdot \hat{\mathbf{r}}_{ij}$, and $c_{ij} \equiv \mathbf{u}_i \cdot \mathbf{u}_j$. Finally, we define the strength anisotropy function as

$$\varepsilon(\hat{\mathbf{u}}_i, \hat{\mathbf{u}}_j, \hat{\mathbf{r}}_{ij}) = \varepsilon_0 \varepsilon_1^\nu(\hat{\mathbf{u}}_i, \hat{\mathbf{u}}_j) \varepsilon_2^\mu(\hat{\mathbf{u}}_i, \hat{\mathbf{u}}_j, \hat{\mathbf{r}}_{ij}), \qquad (6)$$

with μ and ν adjustable exponents,

$$\varepsilon_1(\hat{\mathbf{u}}_i, \hat{\mathbf{u}}_j) = \left[1 - \chi^2 c_{ij}^2\right]^{-\frac{1}{2}}, \qquad (7)$$

and

$$\varepsilon_2(\hat{\mathbf{u}}_i, \hat{\mathbf{u}}_j, \hat{\mathbf{r}}_{ij}) = \Gamma(\chi'), \qquad (8)$$

where

$$\chi' = \frac{(\kappa')^{\frac{1}{\mu}} - 1}{(\kappa')^{\frac{1}{\mu}} + 1}, \qquad (9)$$

and $\kappa' = \varepsilon_e/\varepsilon_f$. Here ε_e represents the potential well depth for an edge–edge configuration, and ε_f the potential well depth for a face–face configuration. Making $\kappa' = 0.2$ in the potential favors the face–face configuration between the discs, so that the nematic and columnar phases are promoted (Fig. 2a).

We will express a set of parameters for the Gay-Berne potential using the notation GB(κ, κ', μ, ν), as proposed by Bates and Luckhurst.[24] Following previous work,[25] the parametrization of the system investigated in this study is GB (0.5, 0.2, 1.0, 2.0). This particular aspect ratio is chosen because the nematic region in the phase diagram for this parametrization covers a wider temperature range as compared to thinner disks,[25] a feature which is also highly desirable from an experimental point of view. Notice that this set of parameters promotes the formation of columns of discs, since the strongest attraction between nematogens happens when their axes are parallel to each other and to the vector that connects their centers.

The wall–disc interaction is also modeled with a Gay-Berne potential[16] of the form

$$V(z,\theta) = \varepsilon_w \left[\frac{2}{15} \left(\frac{\sigma_{ff}}{z - z_{shift}(\theta)} \right)^9 - \left(\frac{\sigma_{ff}}{z - z_{shift}(\theta)} \right)^3 \right]$$
$$\times \left[1 + AP_2(\cos(\theta)) \right], \qquad (10)$$

where $P_2(x) = \frac{1}{2}(3x^2 - 1)$ is the second order Legendre polynomial and ε_w is an energy prefactor which determines the strength of the anchoring with respect to the disc–disc interaction. The function z_{shift} determines the wall–disc contact distance and is defined as

$$z_{shift}(\theta) = 0.5 \left[\sigma_0 \left(1 - \frac{2\chi}{1 + \chi} \cos^2(\theta) \right)^{-\frac{1}{2}} - \sigma_{ff} \right] \qquad (11)$$

The advantage of this model for the wall–disc interaction over others existing in the literature is that it allows the forces and gorques to be calculated in an easy way, in particular for molecular dynamics simulations. It also allows the anchoring energy to be changed as a function of the orientation of the mesogens, and hence the preferred anchoring orientation can be chosen. The type of anchoring at the walls is determined by the value of the parameter A. For example, $A = -0.5$ promotes planar or edge-on anchoring, while $A = 1.0$ encourages homeotropic or face-on anchoring, as depicted in Fig. 2b where we plot $V(z^*,\theta)$ as a function of $z^* = z/\sigma_0$, the distance of the particle to the wall. In this work, we set $\varepsilon_w = 9.0$ for all cases which corresponds to the analogous ratio of interaction between the disc–wall energy and the disc–disc energy used in a previous work.[14] As we will show in the Discussion section, this value for ε_w together with the rest of the system parameters represents

a strong anchoring but within the typical experimental setups.[26–28]

2.2 Simulation details

Molecular dynamics simulations have been carried out on an ensemble of 20 000 particles inside a parallelepipedic box of volume V. The simulation box presents periodic boundary conditions along the x and y directions and is limited along the z axis by two walls which promote one of the two different anchorings: homeotropic or face-on, and planar or edge-on. In these simulations the Nosé–Hoover thermostat/barostat[29] couple was used to fix the temperature of the system and its tangential components of the stress tensors P_{xx}^* and P_{yy}^*, with $P_{xx}^* = P_{yy}^* = 25.0$ which corresponds to the same pressure applied in a similar study developed by Bellier-Castella et al.;[16] only the x–y area of the box was allowed to fluctuate. The thermostat constant was set at $Q_t = 10$, while the barostat constant used was $Q_p = 1000$. It is important to notice that, given that the system has been brought to equilibrium by fixing only the tangential component of the stress tensor, leaving the normal component free, the system's pressure does not remain constant in our annealing process. We have used σ_0 and ε_0 as length and energy units, respectively, and standard reduced units ($T^* = k_B T/\varepsilon_0$, $P^* = P\sigma_0^3/\varepsilon_0$ and $\rho^* = \rho\sigma_0^3$, where k_B stands for the Boltzmann constant) for the rest of the system parameters. Equations of translational and orientational dynamics were integrated using the velocity-Verlet algorithm with a reduced time step of $\delta t = \delta t (\sigma_0^2 m/\varepsilon_0)^{-\frac{1}{2}} = 0.0015$ (where $m = 1$).

In order to study the system's temperature dependence, a system is taken from a high temperature of $T^* = 2.0$ (where the unconfined or infinite system is isotropic) into a low temperature of $T^* = 1.6$ (where the infinite system has turned columnar), through an annealing procedure with ΔT^* steps of 0.02. Simulation runs consisted of $\mathcal{O}(10^6)$ time steps for equilibration for each T^*, followed by production runs of 5×10^6 timesteps for temperatures above 1.84, and 1.7×10^7 timesteps when the systems were below this temperature. In order to discard time-dependant states for this ensemble, control runs with $N = 5000$ particles for up to 2.0×10^7 timesteps were also done. To minimize configurational correlations between measurements, the thermodynamic and structural quantities were calculated every 100 timesteps, from which averages were then determined.

3 Results and discussion

In what follows, results from simulations are presented for four different confined systems: face-on anchoring systems with confinement lengths $L_z^* = 50$ and $L_z^* = 25$, and edge-on anchoring systems with confinement lengths $L_z^* = 50$ and $L_z^* = 25$, where $L_z^* = L/\sigma_0$ is the reduced length; the results for the face-on anchoring system will be presented first, followed by those corresponding to the edge-on anchoring systems.

3.1 Face-on

3.1.1 $L_z^* = 50$. A well-known fact in confined systems is that the anchoring induces a stratification of the fluid, forming
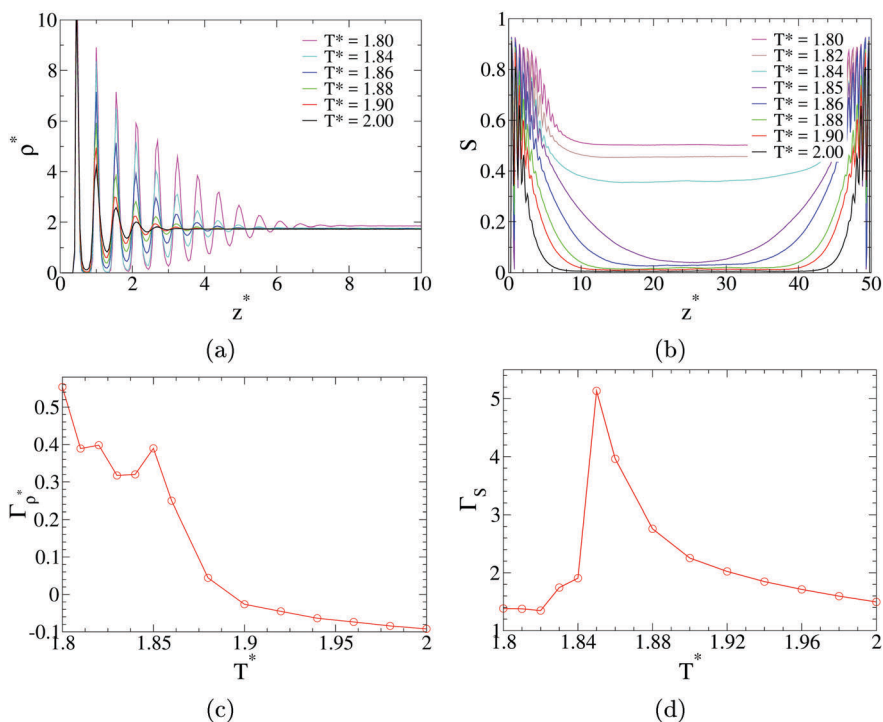
Fig. 3 Results for face-on anchoring with $L_z^* = 50$: (a) density profile in the z-direction for the temperature range $T^* \in [1.80, 2.00]$. (b) Order parameter profile in the z-direction for the same range of temperatures, showing isotropic behaviour for $T^* \geq 1.85$ and nematic behaviour for $T^* \leq 1.84$. (c) Adsorption coefficient Γ_{ρ^*} vs. T^*. Notice the change of the slope of the curve around $T^* = 1.85$ which marks the onset of the isotropic–nematic transition, and (d) orientational adsorption coefficient Γ_S vs. T^*, where the isotropic nematic–transition can be clearly seen.

ordered layers near the wall that gradually lose orientational and translational order as one moves away from the walls. In order to characterize the orientational order of the system, we calculated the largest eigenvalue of the orientational tensor:[30]

$$\mathbf{Q} = \frac{1}{2N}\sum_{i=1}^{N}(3\hat{\mathbf{u}}_i \otimes \hat{\mathbf{u}}_i - \mathbf{I}) \qquad (12)$$

where $\otimes$ denotes the tensor product, $\mathbf{I}$ corresponds to the identity matrix, and N is the total number of particles contained in the system. The normalized eigenvector corresponding to λ_{max} is the system's director $\mathbf{n}$, and $S = \lambda_{max}$ is referred to as the orientational order parameter. If $S = 0$ the liquid crystal is in an isotropic state. As the number of particles whose unit vector along their principal axis aligns with the director increases, the S increases to reach a maximum value $S = 1$ which occurs when all the particles are perfectly aligned with the director. Since the systems under consideration are inhomogeneous due to the layering induced by the walls, then the orientational and positional order of the fluid will be position dependent. In this case, the value of the local order parameter is calculated on thin layers of width $0.05\sigma_0$ along the z direction, and corresponds to the largest eigenvalue of the time average of the orientational tensor on a given slab. Also useful for the structural characterization of the systems is the density profile; we calculated this quantity in the z^* direction using

$\rho^*(z) = N_z/(A_{xy}\mathrm{d}z)$, where N_z is the number of particles in a slab parallel to the wall, A_{xy} is the area of the box in the x–y plane and $\mathrm{d}z$ is the width of the bin, which in this case was also fixed at $0.05\sigma_0$.

The results for the system with $L_z^* = 50$ and face-on anchoring are shown in Fig. 3, where we plot the density (a) and the orientational order parameter (b) as functions of the distance z^*, for several values of T^*. Notice the influence of the anchoring reflected through the presence of a succession of peaks in the density profile. The distance between successive peaks is independent of the temperature; however, the number of peaks is not: as the temperature is lowered the number of peaks increases and the ones that are closer to the wall get more defined, for instance, at the highest temperature of $T^* = 2.00$, the last visible peak appears at a distance of about $3.5\sigma_0$, while for $T^* = 1.80$ the last peak can be distinguished around the value of $z = 7.50\sigma_0$. At larger distances from the walls, the density of the system levels off to a final uniform value. On the other hand, the orientational order promoted by the walls levels off at a distance of about $6.0\sigma_0$ at $T^* = 2.0$, and $18.0\sigma_0$ at $T^* = 1.86$. In this temperature range, all the curves level off at a value $S = 0.0$, which means that at the center of the slab the fluid is isotropic. However, for $T^* = 1.84$ the curve levels off at a value $S = 0.37$ which means that the fluid is in a nematic phase. Similarly, for $T^* = 1.80$ the curve levels off at $S = 0.5$. It is interesting to notice that the inhomogeneous region adjacent to the wall, measured using the orientational order parameter, reaches far more distant
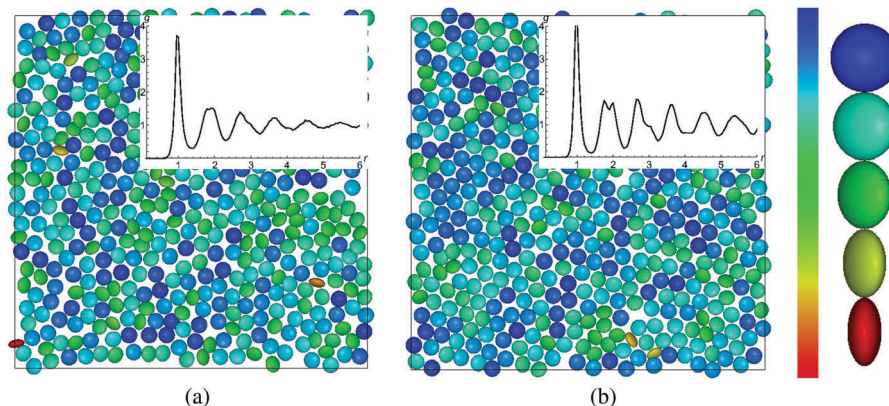
Fig. 4 Snapshots of the particles contained in a layer of thickness $0.5\sigma_0$, adjacent to a wall for face-on anchoring at (a) $T* = 2.00$ and (b) $T* = 1.92$. The insets show their corresponding quasi-two-dimensional radial distribution functions (see the text for further details). The right panel represents the color code for the orientations of the mesogens: the blue particles have their orientation vector parallel to a reference direction; in this figure, the reference direction is perpendicular to the walls (perpendicular to the plane containing the page). Red particles have orientation vectors perpendicular to the same reference direction. All the snapshots presented in this work were obtained with the qmga software.[32]
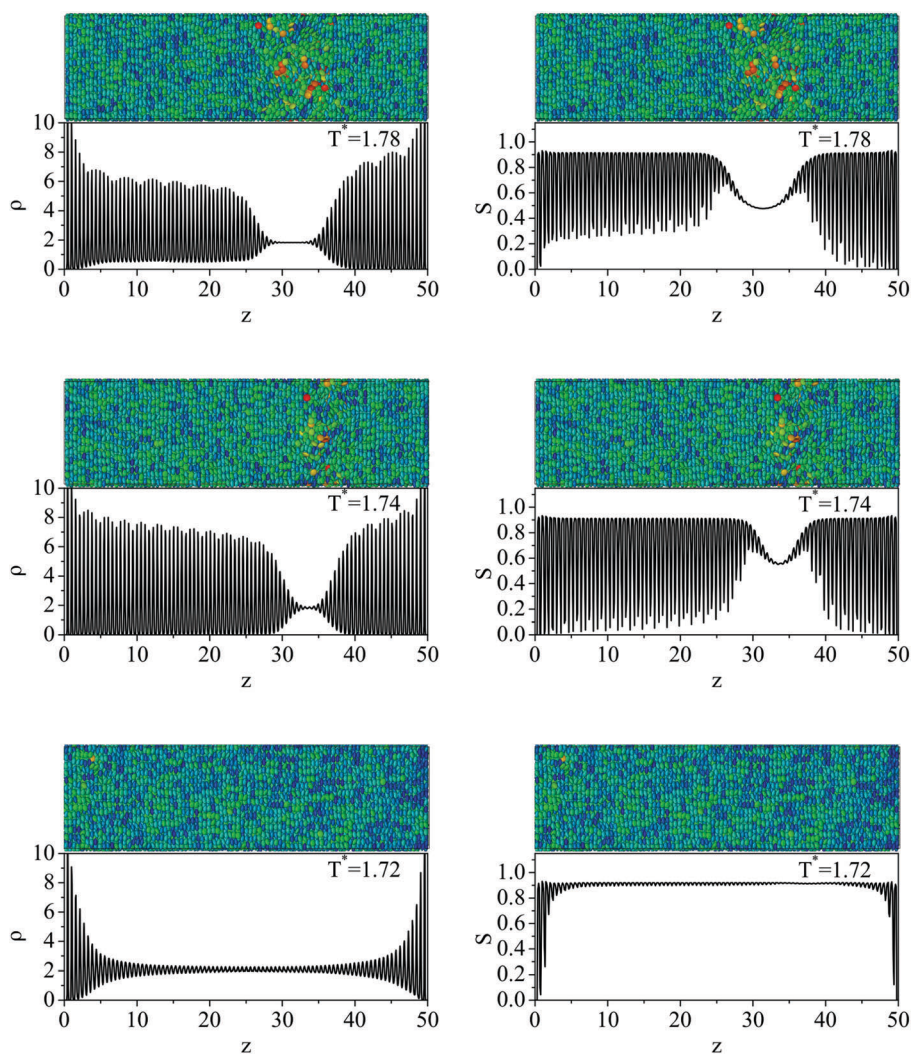
Fig. 5 Density vs. z* (left column) and order parameter vs. z* (right column) for face-on anchoring with $L_z* = 50$ and $T*$ as indicated. The snapshots of the system are also shown above the corresponding $\rho*$ and S curves. The color codes of the snapshots as indicated in Fig. 4 with the reference direction parallel to the z axis.
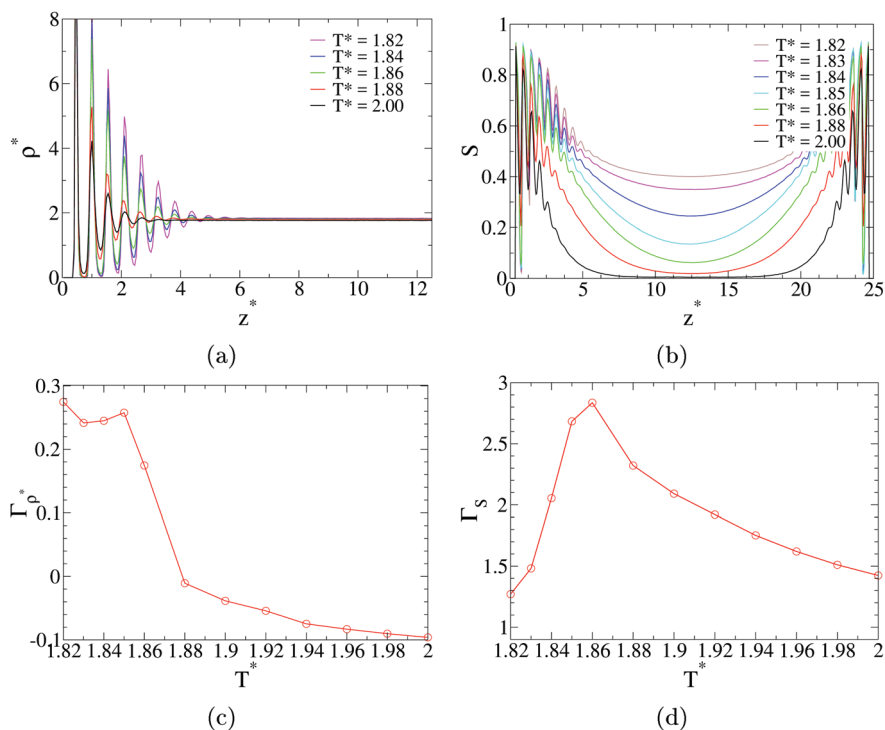
Fig. 6 Results for face-on anchoring with $L_z^* = 25$. (a) Density profile in the z-direction for the temperature range $T^* \in [1.82, 2.0]$ where the system presents isotropic and nematic behaviour. (b) Order parameter profile in the z-direction for the same range of temperatures. (c) Adsorption coefficient Γ_{ρ^*} vs. T^*. (d) Orientational adsorption coefficient Γ_S vs. T^*.

regions toward the center of the slab than those obtained with the density profile. More precisely, for a given temperature, the oscillations in ρ^* and S disappear at about the same value of z^*. However, in contrast to the density that subsequently levels off to its final homogeneous value, the orientational order parameter S does not level off immediately but decreases without further oscillations until it eventually levels off much deeper towards the center of the slabs, especially for the isotropic phase. This will become of primary importance for the more confined systems for, as we will shortly describe, the whole bulk can get trapped in this zone of induced orientation due to the walls. Let us emphasize that in all the cases considered in this section, there is a clearly defined central region of constant density and orientational order parameter that allows this zone to be labelled as the "bulk" region.

We also quantified the layering in the isotropic and nematic regions by calculating the adsorption coefficient Γ_{ρ^*}, defined as:

$$\Gamma_{\rho^*} = \int_{z=0}^{L_z^*/2} \left(\rho^*(z) - \rho^{*B}\right) dz, \qquad (13)$$

where ρ^{*B} stands for the time average density at $z^* = L_z^*/2$. This quantity is a decreasing function of T^* due to the attractive nature of the walls. Fig. 3c shows the values of Γ_{ρ^*} obtained for the range of temperatures of $T^* \in [1.80, 2.00]$, where there are clearly two regions: isotropic for $T^* \geq 1.85$ and nematic region for lower values of T^*. Further indication of the isotropic–nematic

transition can be obtained by calculating an orientational adsorption coefficient Γ_S, defined as:[31]

$$\Gamma_S = \int_{z=0}^{L_z^*/2} \left(S(z) - S^B\right) dz \qquad (14)$$

where S^B stands for the time average order parameter in the central region of the simulation box. Fig. 3d shows the values obtained for the range of temperatures of $T^* \in [1.80, 2.00]$. Notice that for temperatures larger than $T^* = 1.85$, Γ_S is a decreasing function of the temperature. This is consistent with the fact that at higher values of the temperature, the orientational order of the mesogens close to the wall decreases. The nematic part of the curve does not show a clear increasing character because, in this case, S^B is a function of temperature in contrast to ρ^{*B}.

In order to illustrate the positional order that molecules possess within a given layer adjacent to the walls, we calculated a quasi-two dimensional radial distribution function for layers of thickness $0.5\sigma_0$ parallel to the wall, defined as:

$$g(r_{xy}) = \frac{N(r_{xy})}{2\pi r_{xy} dr_{xy}}, \qquad (15)$$

where r_{xy} stands for the xy projection of the distance between two particles, $2\pi r_{xy} dr_{xy}$ stands for the area of a cell of thickness dr_{xy} and $N(r_{xy})$ is the number of particles inside this cell.

Fig. 4 includes the snapshots of the adjacent layer to one wall for $T^* = 2.00$ and $T^* = 1.92$, respectively, and their insets contain the quasi-two dimensional radial distribution function. It is clear that the particles increase their positional order, with the shape of the
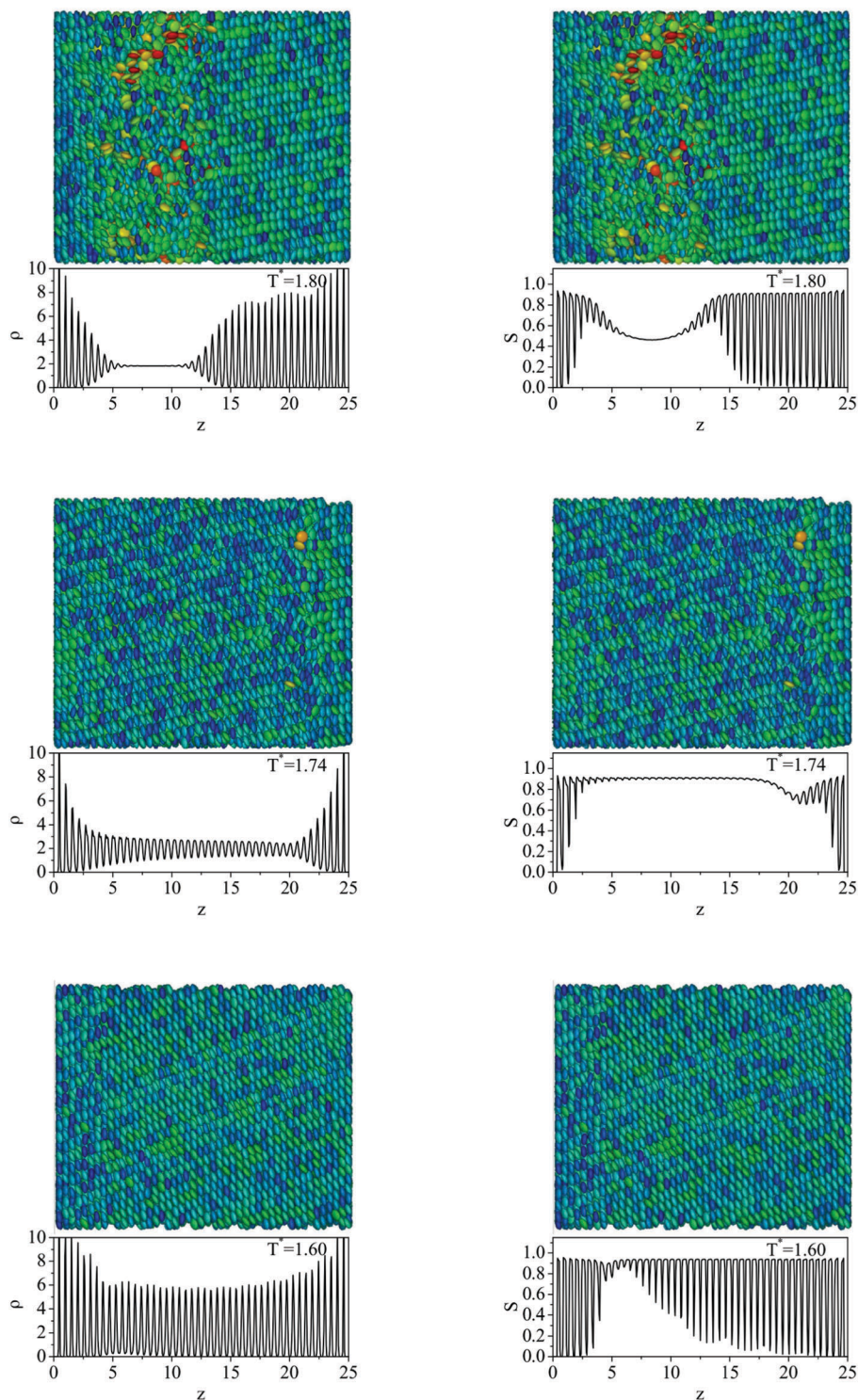
Fig. 7 Density vs. z* (left column) and order parameter vs. z* (right column) for face-on anchoring with L_z^* = 25 and T^* as indicated. Snapshots of the system are also shown above the corresponding ρ^* and S curves. Color codes of the snapshots as indicated in Fig. 4 with the reference direction parallel to the z axis.

$g(r_{xy})$ curve going from a behaviour characteristic of a fluid at T^* = 2.00, to a shape typical of a hexagonal arrangement, as clearly confirmed by the snapshot at $T^* \simeq 1.92$ (Fig. 4a and b, respectively).

For temperatures below T^* = 1.81, we observed a nematic–columnar coexistence region that remained until $T^* \simeq 1.76$.

Fig. 5 shows the density (left column) and order parameter (right column) profiles for three temperatures: T^* = 1.78, 1.74 and 1.72. For these temperatures, the coexistence is clearly recognized in the ρ^* and S profiles of the first two rows (T^* = 1.78 and 1.76), and is also visible in their attached snapshots.
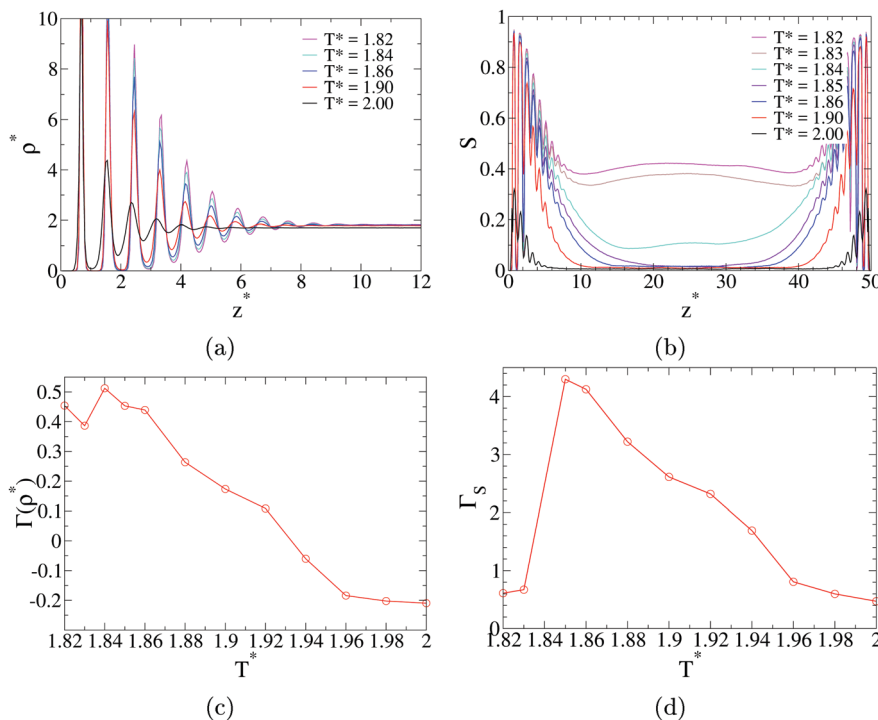
Fig. 8 Results for the edge-on anchoring system with $L_z^* = 50$. (a) Density profile in the z-direction for the temperature range $T^* \in [1.82, 2.00]$ where the system presents isotropic and nematic behaviour. (b) Order parameter profile in the z-direction for the same range of temperatures. (c) Adsorption coefficient Γ_{ρ^*} vs. T^*. (d) Orientational adsorption coefficient Γ_S vs. T^*.

Notice that the position of the nematic region is completely dependent on the immediate state occupied by the system on the phase space; for different initial conditions previous to the transition, the nematic region will be formed at different positions in the cell. However, on average, this phase must remain in the center of the cell. For $T^* = 1.72$ the whole system has turned columnar.

3.1.2 $L_z^* = 25$. The orientational order parameter shows a similar behaviour as before; however, a subtle but important difference appears. At the highest temperature considered, $T^* = 2.00$, the oscillations decay and the overall curve tail levels off to $S = 0.0$ when approaching the center of the slab. However, for $T^* = 1.86$ the tail of the curve extends beyond the middle of the slab, which, combined with the tail corresponding to the second wall, gives as a result that the curve levels off to a value of S different from zero (see Fig. 6b). This is even more evident in the case $T^* = 1.84$, in which the curve levels off to a value of $S \approx 0.25$. In some sense this corresponds to a confinement induced nematic phase (or capillary nematization[33]) which is determined not only by the temperature but also by the width of the cell. For this temperature range, it is not possible to define a homogeneous "bulk" region with a constant orientational order parameter. Furthermore, as shown in Fig. 6d, the orientational order parameter increases continuously with decreasing temperature in contrast to the behaviour of the wider cell, where a jump can clearly be recognized at the isotropic–nematic transition (Fig. 3d).

The effects of the confinement in this smaller system can also be appreciated in the layering effect, *via* the adsorption

coefficients Γ_S and Γ_{ρ^*}, as shown in Fig. 6c and d. Notice that Γ_{ρ^*} is similar as in the $L_z^* = 50$ case, however, Γ_S shows a different behaviour. While in the $L_z^* = 50$ case there is a discontinuity in Γ_S at the isotropic–nematic transition temperature, for the $L_z = 25$ case, although Γ_S still presents a maximum near $T^* = 1.86$, the function in this case is continuous. In this case, the nematic–columnar coexistence region is present for $T^* \in [1.76, 1.81]$. Lowering the temperature below $T^* = 1.76$ turns the system into a columnar phase (Fig. 7).

3.2 Edge-on

3.2.1 $L_z^* = 50$. For the edge-on anchoring system, two main differences appear when compared with the two previous face-on cases: (1) the translational order imposed by the walls extends to longer distances, and (2) there is a lower orientational order at high temperatures, as shown in Fig. 8b. The first difference is the result of the mesogen orientation promoted by the walls, *i.e.*, at a given temperature the density profiles show the same number of peaks for both anchorings, but for the edge-on anchoring the distance between the two consecutive peaks is proportional to σ_0, the minimum distance allowed for two particles approaching on a edge–edge configuration (Fig. 2a). The second difference is related to the fact that we used the same value for the parameter ε_w for both anchorings (eqn (10)): this results in a weaker attraction to the walls for the edge-on anchoring and hence a less oriented fluid at higher temperatures (see Fig. 2b). As in the previous cases, the ordering increases at lower temperatures. The inter-peak separation of the layered structure is larger in the edge-on case, since it is
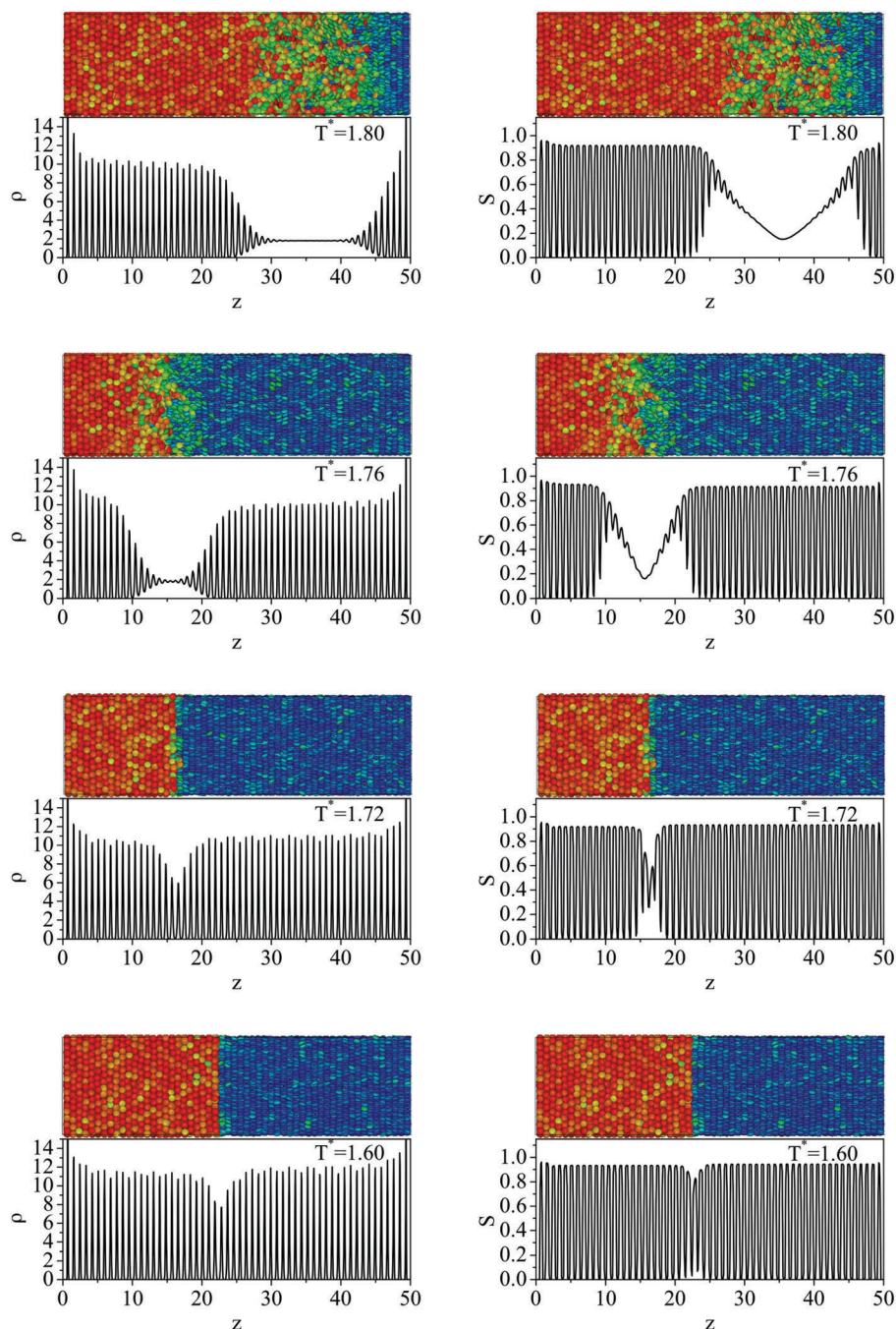
Fig. 9 Density *vs.* z* (left column) and order parameter *vs.* z* (right column) for edge-on anchoring with L_z^* = 50 and T^* as indicated. Snapshots of the system are also shown above the corresponding ρ^* and S curves. Color codes of the snapshots as indicated in Fig. 4 with the reference direction perpendicular to the z axis.

determined by the length of the mesogens perpendicular to the walls, in this case, σ_0, as shown in Fig. 8a. The overall structure of the curves in Fig. 8a and b is the same as in the face-on case.

Fig. 8c shows the values of Γ_{ρ^*} obtained for the range of temperatures of $T^* \in [1.82, 2.00]$; as a general trend, Γ_{ρ^*} is a decreasing function of T^* due to the attractive nature of the walls. Fig. 8d shows the values obtained for the range of temperatures of $T^* \in [1.82, 2.00]$. Notice that for temperatures larger than $T^* = 1.86$, Γ_S is a decreasing function of the

temperature, which is consistent with the fact that at higher values of the temperature, the orientational order of the mesogens close to the wall decreases. The nematic part of the curve does not show a clear increasing character because in this case, S^B is a function of temperature in contrast to ρ^{*B}. Again, a coexistence region is obtained, now for $T^* \in [1.74, 1.80]$.

For lower temperatures of $T^* \in [1.60, 1.72]$, the system turns columnar (Fig. 9). In this case, a disclination is generated; the region that is orientationally frustrated can clearly be
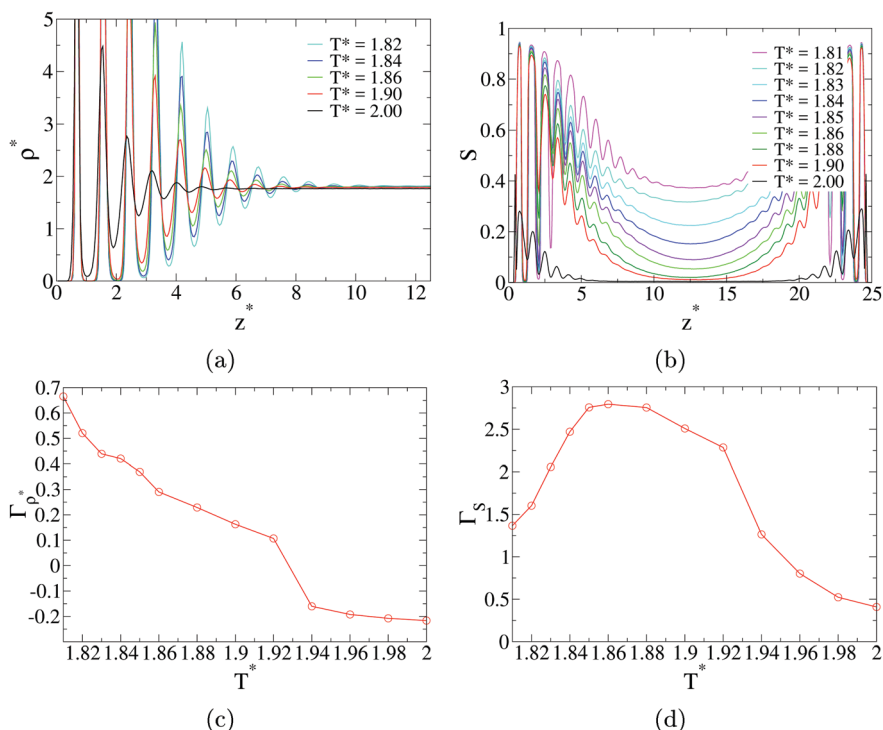
Fig. 10 Results for edge-on anchoring with $L_z{}^* = 25$. (a) Density profile in the z-direction for the temperature range $T^* \in [1.82, 2.0]$ where the system presents isotropic and nematic behaviour. (b) Order parameter profile in the z-direction for the same range of temperatures. (c) Adsorption coefficient Γ_{ρ^*} vs. T^*. (d) Orientational adsorption coefficient Γ_S vs. T^*.

distinguished in the last two rows of snapshots in Fig. 9. In this case, the disclination is reinforced by the fact that the orientation of the mesogens at the walls is uncorrelated, in contrast to the face-on case where, for a perfect alignment, there is only one way for the mesogens to orient, with their $\hat{u}$ vector perpendicular to the walls. On the other hand, the degeneracy of the edge-on case in the wall–disc potential led to edge-on configurations that admit a whole range of orientations, all of them satisfying $\hat{u}$ parallel to the walls.

The formation of a frustrated region trapped between the two columns growing from the walls, has been previously described in ref. 16, were the authors showed that if the two layers adjacent to the wall were properly alligned, the nematic–columnar transition was defect-free. In other words, the orientational order promoted by each wall of the system is independent of the other and, at the transition temperature, this could turn into a competition between the orientations promoted by each wall.

3.2.2 $L_z{}^* = 25$. Fig. 10 shows the profiles for the edge-on anchoring with $L_z{}^* = 25$ at temperatures above 1.82: at temperatures greater than or equal to 1.90, the system presents a homogeneous-isotropic bulk central region with constant density and constant order parameter with an average value around 0.0. At such temperatures, this smaller system presents the same behaviour as the larger system. At $T^* = 1.90$ the order parameter levels off at approximately the center of the slab (Fig. 10b), and for lower temperatures in the range of $T^* \in [1.81, 1.92]$, similar behaviour as in the previous smaller case is found.

Fig. 10c and d present the results obtained for the adsorption coefficients of this system in the temperature range of $T^* \in [1.81, 2.00]$. Notice that, as in the face-on case, Γ_{ρ^*} is similar in both confinement lengths but Γ_S is not. In the $L_z{}^* = 50$ case, there is a discontinuity in Γ_S at the isotropic–nematic transition temperature, and for $L_z{}^* = 25$, Γ_S is a continuous function.

When the temperature is lowered to $T^* = 1.80$, a nematic-columnar coexistence region is obtained and it remains until $T^* = 1.76$ (first two rows in Fig. 11). And for $T^* \leq 1.74$, the system turns columnar.

3.3 Discussion

Fig. 12a presents the T vs. ρ^* phase diagram for the GB(0.5, 0.2, 1.0, 2.0) fluid considered in an unbounded (not confined) region. This diagram was obtained with *NPT* simulations for 2000 particles at the isobars labeled in Fig. 12a, and control runs with 20 000 particles were also done to discard finite size effects for a selected isobar of $P^* = 25.0$. Observe that for every pressure, the isotropic (denoted by circles) and columnar (denoted by asterisks) phases are clearly separated by a nematic region (denoted by triangles). If we specifically focus on the isobar of $P^* = 25.0$, which would be in some sense similar to our $P_{xx}{}^* = P_{yy}{}^* = 25.0$ system, then the isotropic phase is obtained for $T^* \gtrsim 1.86$; the nematic phase is obtained for $T^* \in [1.68, 1.84]$; and the columnar phase is obtained when $T^* \lesssim 1.64$. We would like to point out that the reason for using a thicker mesogen than other models used in the literature[34] obeys to the fact that the
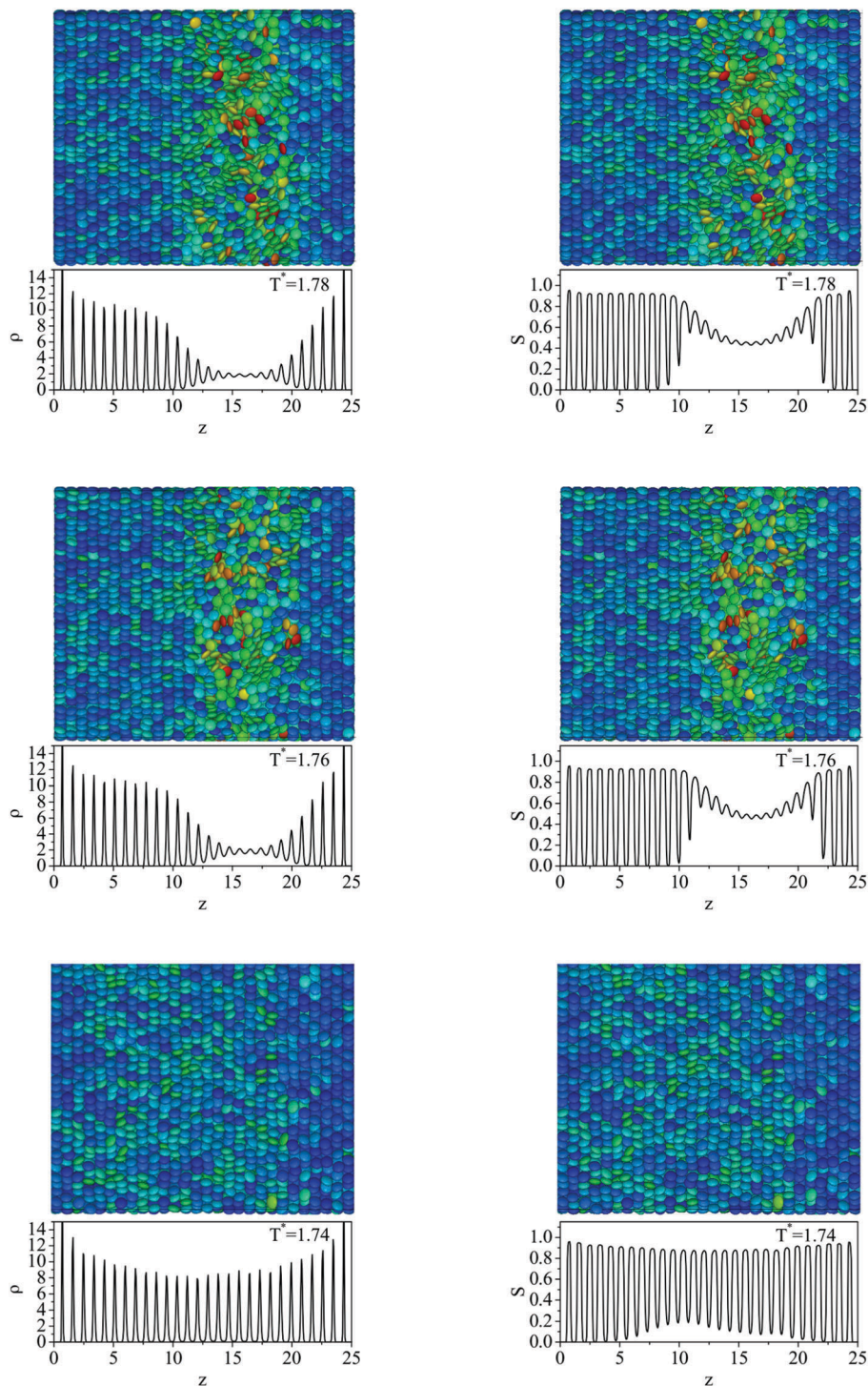
Fig. 11 Density *vs.* z^* (left column) and order parameter *vs.* z^* (right column) for edge-on anchoring with $L_z^* = 25$ and T^* as indicated. Snapshots of the system are also shown above the corresponding ρ^* and S curves. Color codes of the snapshots as indicated in Fig. 4 with the reference direction perpendicular to the z axis.

nematic region in the phase diagram covers a wider temperature range. Although real discotic mesogens are thinner, we believe that mesogens with aspect ratios similar to the one we are using as a model can be synthesized in the future. In order to appreciate the effects of confinement, we compare our results for the confined systems with these isobar results where $P^* = 25.0$.

The corresponding region of the T^*–ρ^* plane is included in two graphics: Fig. 12b corresponds to the comparison of the infinite system *vs.* the larger systems ($L_z^* = 50$) and both anchorings (face-on and edge-on results are represented by blue and red symbols, respectively), while Fig. 12c presents the comparison with the smaller systems ($L_z^* = 25$). Notice that the direct
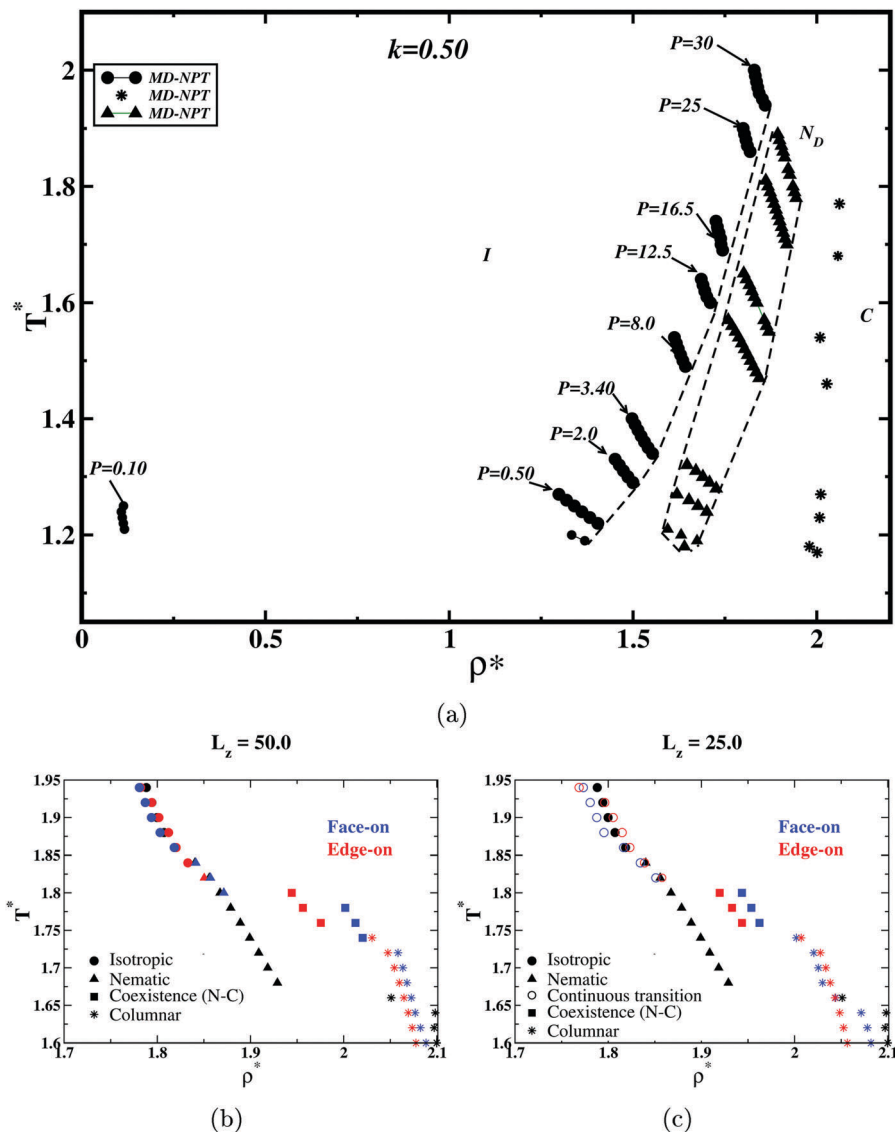
Fig. 12 (a) Phase diagram of the unconfined system, obtained with *NPT* simulations for an ensemble of 2000 particles. The circles represent the isotropic phase, triangles stand for nematic phase and asterisks represent the columnar phase (the same configuration of symbols is used for (b) and (c)). (b) Insets of the phase diagram for the region that contains the results for the confined-systems with $L_z^* = 50$: face-on and edge-on are represented by blue and red symbols, respectively. The squares represent the nematic–columnar (N–C) coexistence region. (c) Corresponding results for the confined-systems with $L_z^* = 25$. Results for the face-on and edge-on systems are plotted in blue and red, respectively, and open circles are used to represent the isotropic and nematic phases which are linked by the continuous isotropic–nematic transition (see Sections 3.1.2 and 3.2.2 for further details).

comparison of $P_{xy}^* = 25.0$ *versus* $P^* = 25.0$ is more qualitative than quantitative, since in the confined systems the pressure is not fixed but rather only the tangential component of the stress tensor P_{xy}^*, which results in a variable (below 25.0) value of P_z^*.

With regard to the results of the larger systems (Fig. 12b), the anchoring does not modify significantly the range of temperatures where the isotropic phase is obtained (observe the black, blue and red circles, which stand for the isotropic phase in the infinite, face-on and edge-on systems, respectively): for the face-on case the last temperature where the isotropic phase is obtained, matches exactly with that obtained in the infinite system ($T^* = 1.86$); for the edge-on case, the system remains isotropic until $T \simeq 1.84$. The triangles on the

phase diagram represent the nematic phase. Notice that in the infinite system there is a wider region of temperatures where the nematic phase is obtained ($T^* \in [1.66, 1.84]$), when compared with the confined system. Indeed, for the face-on case, we found three temperatures where the system is nematic ($T^* \in [1.80, 1.84]$), and only one temperature ($T^* = 1.82$) in the edge-on case. Below the range of temperatures where the nematic region is obtained, we observed a nematic-columnar coexistence region: $T^* \in [1.76, 1.81]$ for the face-on case and $T^* \in [1.76, 1.80]$ for the edge-on case. This coexistence region can be observed in the first two rows of snapshots included in Fig. 5 and 9. For lower temperatures, all the systems turn to columnar (asterisks in Fig. 12b). Notice, though, that for the
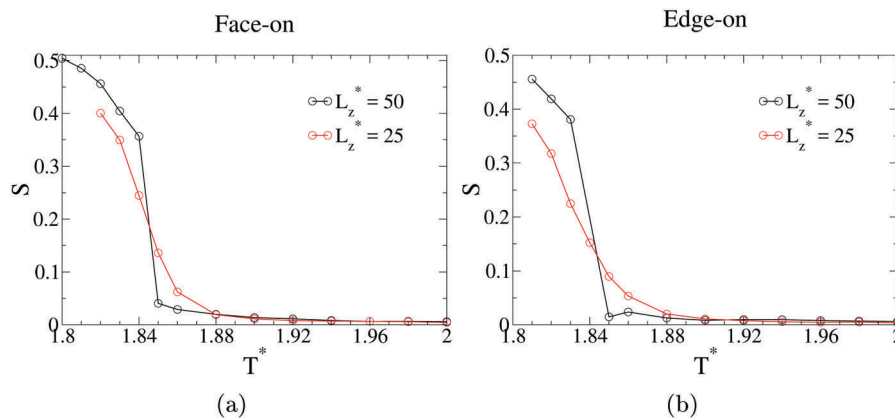
Face-on   Edge-on

Fig. 13 Results of the time average order parameter at the center of the cell for $T^* \in [1.8, 2.0]$ without considering the temperatures where the system turns columnar: (a) face-on and (b) edge-on.

edge-on system, a disclination line is formed due to the incompatibility of the orientations promoted by each wall. This transition provokes a sharp increment of the average density in all the systems. Also, notice that, independently of the anchoring, the nematic–columnar transition temperature of the two less confined systems is higher than the transition temperature for the infinite system.

For the two more confined systems, a very similar behaviour is observed (Fig. 12c). Observe that, as has been previously discussed, a continuous isotropic–nematic transition takes place and it is not possible to separate the isotropic and nematic phases. In order to emphasize this change from first order to continuous, Fig. 13 shows the time average order parameter calculated at the center of the cell for a range of temperatures around the isotropic–nematic transition. Clearly, for the wider cells there is a discontinuity in S, in contrast to the thinner cells for which the curve of S is continuous.

In order to compare the results from our simulations with experimental data, here we present some estimates for the dimensionless parameters used in the simulations. First, notice that all the interesting phenomena observed in this work are around $T^* \equiv k_B T/\varepsilon_0 \simeq 2$. Assuming room temperature, then $\varepsilon_0 \simeq 2 \times 10^{-21}$ Joules. With this energy value we can estimate the anchoring energy, since the adsorption energy per particle, defined by the minimum of the wall–disc potential, is $E_A \simeq 15\varepsilon_0$ (according to Fig. 2b, for the face-on case). In order to transform the surface energy density, let us consider the area of a nematogen in contact with a wall as approximately $A = \pi\sigma_0^2/4$ and a value of $\sigma_0 = 40$ Angstroms, which corresponds to the diameter of a triphenylene-based molecule.[35] This results in a surface energy density of 2×10^{-3} Joules m^{-2}, which is close to the highest experimental measured anchoring energy, where the experimental values range from 10^{-6} J m^{-2} to 10^{-3} J m^{-2}.[26,36] With respect to the size of the cells, the largest length in z of the cell corresponds to $L_z^* = 50\sigma_0 = 200$ nm, and $L_z^* = 25\sigma_0 = 100$ nm for the less confined systems. Notice that these values are again near to the experimental values for confined liquid crystals, which range from confinement lengths of 10 nm to 200 nm.[37,38] Finally, considering a value for the reduced

pressure of $P^* \equiv P\sigma_0^3/\varepsilon_0 \simeq 25$ results in an approximated pressure of 8×10^5 Pascals which is well within the reach of experiments done with liquid crystals under high pressure (8×10^7 according to ref. 39).

4 Conclusions

In this numerical study we have discussed the effects that confinement has on the mesophases of a discotic liquid crystal. A slab geometry with two different anchorings, face-on and edge-on, and two different widths for the slab were analyzed. This was achieved by using an ensemble that kept the distance between the walls and the tangential stress tensor components fixed. As expected, we observed that the orientational order promoted by the walls extends beyond the range of the oscillations that appear on the density counterpart. As a consequence, smaller slabs may inhibit the decay of the order parameter to its isotropic value, thus giving rise to an inhomogeneous phase that spans the central region of the slab. For the cases where these inhomogeneous phases are present, the isotropic–nematic transition is a continuos transition, in agreement with previous theoretical predictions.[40] This happens in contrast to the less confined systems, where the central region of the slab changes from isotropic to nematic without taking intermediate values of the order parameter.

When compared with the behaviour of the infinite/free system, our results show that the anchoring has a significant impact on the nematic phase: in all confined systems the range of temperatures where this phase is present is reduced, and for the edge-on anchoring systems this reduction is particularly noticeable. In other words, the anchoring of the walls destabilizes the nematic phase in favor of the columnar phase.

Finally, a planar anchoring induces a longer ranged orientational correlation, as compared to the homeotropic anchoring, and this is reflected in a higher nematic–columnar transition temperature.

Notice that according to our results for the edge-on $L_z^* = 50$ case, a defect is generated when the system turns columnar due

to the incompatibility of the orientations promoted by the walls. This orientationally frustrated region has been previously reported in ref. 16, for a system where the orientation promoted by the layers growing from each wall is different.

Conflicts of interest

There are no conflicts of interest to declare.

Acknowledgements

References

1 M. Heuberger, M. Zäch and N. D. Spencer, *Science*, 2001, **292**, 905–908.
2 M. Alcoutlabi and G. B. McKenna, *J. Phys.: Condens. Matter*, 2005, **17**, R461–R524.
3 R. Evans, *J. Phys.: Condens. Matter*, 1990, **2**, 8989–9007.
4 K. E. Gubbins, Y. Long and M. Sliwinska-Bartkowiak, *J. Chem. Thermodyn.*, 2014, **74**, 169–183.
5 S. Granick, *Science*, 1991, **253**, 1374–1379.
6 B. Jerôme, *Rep. Prog. Phys.*, 1991, **54**, 391–451.
7 S. H. Ryu and D. K. Yoon, *Liq. Cryst.*, 2016, **43**, 1951–1972.
8 R. van Roij, M. Dijkstra and R. Evans, *J. Chem. Phys.*, 2000, **113**, 7689–7701.
9 M. Bremer, P. Kirsch, M. Klasen-Memmer and K. Tarum, *Angew. Chem., Int. Ed.*, 2013, **52**, 8880–8896.
10 D. Franklin, Y. Chen, A. Vazquez-Guardado, S. Modak, J. Boroumand, D. Xu, S.-T. Wu and D. Chanda, *Nat. Commun.*, 2015, **6**, 7337.
11 Y. J. Liu and X. W. Sun, *Appl. Phys. Lett.*, 2007, **90**, 191118.
12 T. Gruhn and M. Schoen, *Mol. Phys.*, 1998, **93**, 681–692.
13 M. Greschek, M. Melle and M. Schoen, *Soft Matter*, 2010, **6**, 1898–1909.
14 E. Cañeda-Guzmán, J. A. Moreno-Razo, E. Díaz-Herrera and E. J. Sambriski, *Mol. Phys.*, 2014, **112**, 1149–1159.
15 J. C. Armas-Pérez, X. Li, J. A. Martínez-González, C. Smith, J. P. Hernández-Ortiz, P. F. Nealey and J. J. de Pablo, *Langmuir*, 2017, **43**, 12516–12524.
16 L. Bellier-Castella, D. Caprion and J.-P. Ryckaert, *J. Chem. Phys.*, 2004, **121**, 4874–4883.

17 D. Caprion, *Eur. Phys. J. E: Soft Matter Biol. Phys.*, 2009, **28**, 305–313.
18 R. Busselez, C. V. Cerclier, M. Ndao, A. Ghoufi and R. Lefort, *J. Chem. Phys.*, 2014, **141**, 134902.
19 T. Wöhrle, I. Wurzbach, J. Kirres, A. Kostidou, N. Kapernaum, J. Litterscheidt, J. C. Haenle, P. Staffeld, A. Baro, F. Giesselmann and S. Laschat, *Chem. Rev.*, 2016, **116**, 1139–1241.
20 T. Seki, S. Nagano and M. Hara, *Polymer*, 2013, **54**, 6053–6072.
21 J. Hoogboom, J. A. A. W. Elemans, T. Rasing, A. E. Rowan and R. J. M. Nolte, *Polym. Int.*, 2007, **56**, 1186–1191.
22 Y. Yi, M. Nakata, A. R. Martin and N. A. Clark, *Appl. Phys. Lett.*, 2007, **90**, 163510.
23 D. J. Cleaver, C. M. Care, M. P. Allen and M. P. Neal, *Phys. Rev. E: Stat. Phys., Plasmas, Fluids, Relat. Interdisc. Top.*, 1996, **54**, 559–567.
24 M. A. Bates and G. R. Luckhurst, *J. Chem. Phys.*, 1999, **110**, 7087–7108.
25 O. Cienega-Cacerez, C. García-Alcántara, J. A. Moreno-Razo, E. Díaz-Herrera and E. J. Sambriski, *Soft Matter*, 2016, **12**, 1295–1312.
26 M. Rahimi, T. F. Roberts, J. C. Armas-Pérez, X. Wang, E. Bukusoglu, N. L. Abbott and J. J. de Pablo, *PNAS*, 2015, **112**, 5297–5302.
27 K. Kocevar and I. Musevic, *Liq. Cryst. Today*, 2003, **112**, 3–8.
28 A. Marino, V. Tkachenko, E. Santamato, N. Bennis, X. Quintana, J. M. Otón and G. Abbate, *J. Appl. Phys.*, 2010, **107**, 073109.
29 J. M. Ilnytskyi and M. R. Wilson, *Comput. Phys. Commun.*, 2002, **148**, 43–58.
30 R. Eppenga and D. Frenkel, *Mol. Phys.*, 1984, **52**, 1303–1334.
31 M. M. Pineiro, A. Galindo and A. O. Parry, *Soft Matter*, 2007, **3**, 768–778.
32 A. T. Gabriel, T. Meyer and G. Germano, *J. Chem. Theory Comput.*, 2008, **4**, 468–476.
33 H. Reich and M. Schmidt, *J. Phys.: Condens. Matter*, 2008, **19**, 326103.
34 M. A. Bates and G. R. Luckhurst, *J. Chem. Phys.*, 1996, **104**, 6696.
35 S. K. Pal, S. Setia, B. S. Avinash and S. Kuma, *Liq. Cryst.*, 2013, **40**, 1769–1816.
36 O. Lavrentovich, B. Lev and A. Trokhymchuk, *Condens. Matter Phys.*, 2010, **13**, 30101.
37 G. Carbone, G. Lombardo, R. Barberi, I. Musevic and U. Tkalec, *Phys. Rev. Lett.*, 2009, **103**, 167801.
38 R. Zhang, X. Zeng, B. Kim, R. J. Bushby, K. Shin, P. J. Baker, V. Percec, P. Leowanawat and G. Ungar, *ACS Nano*, 2015, **9**, 1759–1766.
39 R. V. Tranfield and P. J. Collins, *Phys. Rev. A: At., Mol., Opt. Phys.*, 1982, **25**, 2744–2749.
40 P. Sheng, *Phys. Rev. Lett.*, 1976, **37**, 1059–1062.